



Delft University of Technology

B-spline function-based approach for GPS tropospheric tomography

Haji-Aghajany, Saeid; Amerian, Yazdan; Verhagen, Sandra

DOI

[10.1007/s10291-020-01005-x](https://doi.org/10.1007/s10291-020-01005-x)

Publication date

2020

Document Version

Accepted author manuscript

Published in

GPS Solutions

Citation (APA)

Haji-Aghajany, S., Amerian, Y., & Verhagen, S. (2020). B-spline function-based approach for GPS tropospheric tomography. *GPS Solutions*, 24(3), Article 88. <https://doi.org/10.1007/s10291-020-01005-x>

Important note

To cite this publication, please use the final published version (if applicable). Please check the document version above.

Copyright

Other than for strictly personal use, it is not permitted to download, forward or distribute the text or part of it, without the consent of the author(s) and/or copyright holder(s), unless the work is under an open content license such as Creative Commons.

Takedown policy

Please contact us and provide details if you believe this document breaches copyrights. We will remove access to the work immediately and investigate your claim.

1 **B-spline function-based approach for GPS tropospheric tomography**

2 Saeid Haji-Aghajany^{a,b}, Yazdan Amerian^a, Sandra Verhagen^b

3 ^aFaculty of Geodesy and Geomatics Engineering, K. N. Toosi University of Technology, Tehran,
4 Iran

5 ^bFaculty of Civil Engineering and Geosciences, Delft University of Technology, Stevinweg 1,
6 2628 CN Delft, The Netherlands

7 s_h_aghajany@mail.kntu.ac.ir, S.HajiAghajany@tudelft.nl, amerian@kntu.ac.ir,
8 sandra.verhagen@tudelft.nl

9

10 **Abstract** Tropospheric tomography is one of the most important techniques to reconstruct three
11 dimensional (3D) images of the tropospheric water vapor fields using a local GNSS network. In
12 the conventional tropospheric tomography method, called voxel-based tropospheric tomography,
13 the 3D space is divided into many voxels and the amount of water vapor is estimated for each
14 voxel. This method suffers from three disadvantages. First, it needs empirical constraints in order
15 to fix the rank deficiency of the coefficient matrix. Second, the amount of water vapor is assumed
16 to be constant in the 3D space of a voxel despite the large spatial variations of this parameter.
17 Third, the number of unknown parameters is high compared to the number of observations.
18 Therefore, an approach based on mathematical functions, called function-based tropospheric
19 tomography, is presented to overcome these problems. The tropospheric tomography using the
20 voxel-based and function-based approaches is performed using 17 GPS stations and different
21 weather conditions have been considered. Radiosonde observations and GPS positioning results
22 are used to validate the obtained results. Comparison of the results with the radiosonde data
23 indicates that the use function-based method reduces the mean RMSE by about 0.3 gr/m³.
24 Validation using positioning shows that in wet weather conditions, the difference between the
25 RMSE of the two approaches is significant. All the validations show the ability and applicability
26 of the function-based tropospheric tomography approach.

27

28 **Keywords:** GPS, Tropospheric tomography, Water vapor, Function-based, B-spline

29

30 **Introduction**

31 The spatiotemporal distribution of water vapor is very important in numerical weather forecasting
32 and disastrous-weather monitoring. There are many instruments for measuring water vapor, such
33 as radiosonde, water vapor radiometer, and meteorological satellites and sensors (Merrikhpour and
34 Rahimzadegan 2017; Merrikhpour and Rahimzadegan 2019). These instruments have low
35 spatiotemporal resolution and high cost and are dependent on weather conditions. In recent years,
36 the GNSS tropospheric tomography has been used to retrieve the 3D distribution of water vapor
37 and to overcome the mentioned drawback of the instruments. The first GNSS tropospheric
38 tomography experiments to obtain wet refractivity were performed by Flores and Hirahara (Flores
39 et al. 2000; Hirahara 2000). In the following years, many researchers have tried to improve the
40 accuracy and performance of this technique (Bender et al. 2011; Perler et al. 2011; Rohm et al.
41 2014; Yao and Zhao 2016; Haji-Aghajany and Amerian 2017; Haji-Aghajany and Amerian 2018;
42 Zhao et al. 2018a; Heublein et al. 2019).

43 In voxel-based tropospheric tomography, due to the geometric distribution of GNSS
44 receiver and the constellation of GNSS satellites, some voxels are not crossed by any ray. This
45 problem causes a rank deficiency in the coefficient matrix. Some previous researchers proposed
46 the methods of using the signals penetrating from the side face of tomography area (Yao and Zhao
47 2016; Zhao and Yao 2017; Zhao et al., 2020) and using the data of GNSS observations outside the
48 study area to solve this problem (Zhao et al., 2019). However, in general, the use of constraints to
49 solve the problem is inevitable. Some researchers have suggested approaches to add constraints to
50 the tropospheric tomography problem (Flores et al. 2000; Troller et al. 2002; Rohm and Bosy
51 2009; Bender et al. 2011). These empirical constraints sometimes cause the reconstructed water
52 vapor field to deviate from the correct distribution. Considering the amount of water vapor fixed
53 everywhere in the 3D space of a voxel and the high number of unknown parameters compared to
54 the number of observations are other drawbacks of the conventional tropospheric tomography
55 method. The high number of unknown parameters reduces the stability of the tomography model.

56 The first function-based tropospheric tomography studies of water vapor have been
57 performed by Zhao et al. (2018b). He used the fix-degree polynomial function for different vertical
58 layers. A high-degree polynomial as an interpolant function oscillates between data points and at
59 the edges of an interval and reduces the accuracy of modeling. We present a new method based on

60 the non-identical degrees of the B-spline scaling function to overcome the disadvantages of the
 61 voxel-based and polynomial function-based methods. The B-spline function has already been used
 62 in ionosphere tomography and has shown high ability in ionosphere modeling (Amerian et al.
 63 2013a, b). Here, the B-spline scaling function with different degrees and resolution levels is used
 64 in the tropospheric tomography.

65 Function-based tropospheric tomography avoids the use of empirical constraints, and only
 66 an a priori constraint is needed to reconstruct the vertical distribution of water vapor. Moreover, it
 67 reduces the number of unknown parameters. To perform the tomography, we used the observations
 68 of 17 GPS stations for 30 different days under different weather conditions. After applying the
 69 voxel-based and function-based methods, the results are validated using the GNSS positioning
 70 technique and radiosonde observations. In the following, the basics of the voxel-based and
 71 function-based tropospheric tomography are provided. Then, the study area, data set, and the
 72 obtained results from the two tomography approaches are presented. Validation and discussion are
 73 presented in the last section.

74

75 Tropospheric tomography technique

76 The slant water vapor (SWV) is the total water vapor content from satellite to receiver. This can
 77 be one of the input data types of the tomography problem and is expressed as follows (Braun
 78 2004):

$$79 \quad SWV = \int_{\text{Rec.}}^{\text{Sat.}} \rho(s) ds \quad (1)$$

80 where s represents the path of the ray, and ρ is the water vapor density (WVD). Equation (1) is the
 81 fundamental relation of the tropospheric tomography problem. The SWV can be obtained by the
 82 following formula (Bevis et al. 1992):

$$83 \quad SWV = \frac{10}{R_w [(k_3 / T_m) + k_2]} SWD \quad (2)$$

84 where $k_2' = 16.48 \text{ KhPa}^{-1}$, $k_3 = 3.776 \times 10^5 \text{ K}^2 \text{hPa}^{-1}$ and $R_w = 461 \text{ JKg}^{-1} \text{K}^{-1}$ are refractivity coefficients. T_m is
 85 weighted mean tropospheric temperature and SWD is the slant wet delay of the ray which can be
 86 computed using (Davis et al. 1993):

$$87 \quad SWD = (mf_{wet} \times ZWD) + (mf_{wet} \times \cot(\alpha) \times ((G_{NS}^W \times \cos az) + (G_{EW}^W \times \sin az))) + R \quad (3)$$

88 where G_{NS}^W and G_{EW}^W are non-hydrostatic delay gradients in N-S and E-W directions, mf_{wet} is non-
 89 hydrostatic mapping function, α is satellite elevation and az is the azimuth. ZWD is the zenith
 90 wet delay, which can be estimated by subtracting the zenith hydrostatic delay (ZHD) from the
 91 zenith total delay (ZTD). ZHD can be computed accurately using the following model
 92 (Saastamoinen 1973):

$$93 \quad ZHD = \frac{0.002277 P_s}{(1 - 0.00266 \cos(2\varphi) - 0.00000028 H)} \quad (4)$$

94 where φ and H are the latitude and height and P_s is the surface pressure. In the following, the
 95 theory of voxel-based and function-based tomography are described.

96

97 Voxel-based method

98 The tomography area is divided into several voxels in which the WVD is considered a constant
 99 during the specified period of time. Therefore, the equation between the SWV and the WVD can
 100 be discretized as follows (Chen and Liu 2014):

$$101 \quad SWV^P = \sum_i^n \sum_j^m \sum_k^q d_{i,j,k}^P \rho_{i,j,k} \quad (5)$$

102 where n , m and q is the number of voxels in the latitudinal, longitudinal, and vertical directions, P
 103 is the counter of rays, $d_{i,j,k}^P$ is the distance traveled by the ray P in the voxel (i, j, k) and $\rho_{i,j,k}$ is the
 104 WVD in the voxel (i, j, k) . Equation (5) in matrix form is:

$$105 \quad {}_T L_1 = {}_T A_{nmq} \rho_1 \quad (6)$$

106 where T is the number of the GNSS rays, A is the coefficient matrix and ρ is the vector of unknown
 107 WVD. An inversion algorithm needs to be applied to solve the unknown parameters. As previously

108 mentioned, in voxel-based tomography, the coefficient matrix is a large sparse matrix, and not all
 109 of the unknowns can be estimated. Therefore, adding constraints using various approaches to solve
 110 this problem is inevitable (Flores et al. 2000; Troller et al. 2002; Rohm and Bosy 2009; Bender et
 111 al. 2011). As a result, the accuracy of the results is influenced since the additional constraint cannot
 112 completely satisfy the actual situation. In this study, the horizontal constraints are performed based
 113 on the assumption that the WVD in a voxel is a mean value of its horizontally nearest neighbors
 114 (Yao and Zhao 2016). In order to form the vertical constraints, the negative exponential function
 115 is used (Flores et al. 2000).

116 The model resolution matrix is used to select the optimal resolution and geometry for the
 117 tomography model (Haji-Aghajany and Amerian 2017). The 3D ray-tracing technique is used to
 118 compute the distance traveled by the rays in each voxel. More details about this technique can be
 119 found in Haji-Aghajany and Amerian (2017). The tropospheric tomography is a large and ill-
 120 conditioned inverse problem due to the high number of observations and a wide area of modeling.
 121 Therefore the use of regularization methods is necessary. We use the least-squares QR (LSQR)
 122 iterative regularization method (Haji-Aghajany and Amerian 2017; Haji-Aghajany and Amerian
 123 2018).

124

125 Function-based method

126 In previous studies, the study area was divided into many voxels, which caused problems in the
 127 determination of the WVD. In the function-based tropospheric tomography, the study area is not
 128 divided in the horizontal direction, and only a few vertically layers are needed. In this method, the
 129 WVD for each layer is expressed as a function:

$$130 \quad \rho = F(\lambda, \varphi) \tag{7}$$

131 where λ and φ are the longitude and latitude of intersection between the ray and the center of the
 132 layer. Therefore, the SWV for i -th layer in P -th ray direction can be written as:

$$133 \quad SWV_i^P = \rho_i \cdot d_i^P = F(\lambda_i, \varphi_i) \cdot d_i^P \tag{8}$$

134 where ρ_i is the WVD for the location of (λ_i, φ_i) and d_i^P is the distance travel by the P -th ray in i -
 135 th layer. The SWV can be transformed as follows:

136 $SWV^P = SWV_1^P + SWV_2^P + \dots + SWV_n^P$ (9)

137 Using to equation (8), this can be written as follows:

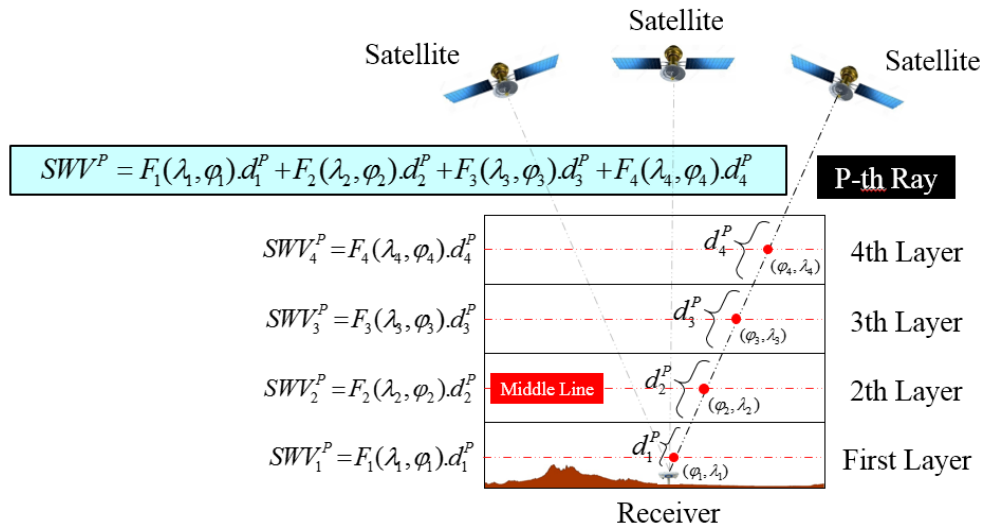
138 $SWV^P = F(\lambda_1, \varphi_1).d_1^P + F(\lambda_2, \varphi_2).d_2^P + \dots + F(\lambda_n, \varphi_n).d_n^P$ (10)

139 where n is the number of layers. It is clear that the distribution of WVD at the different elevation
 140 layers is not the same. Therefore, it is better to use various degree functions for different layers.
 141 Accordingly, equation (10) can be written as follows:

142 $SWV^P = F_1(\lambda_1, \varphi_1).d_1^P + F_2(\lambda_2, \varphi_2).d_2^P + \dots + F_n(\lambda_n, \varphi_n).d_n^P$ (11)

143 Basic schematic diagram of this method can be seen in Fig.1.

144



145

146 **Fig. 1** Schematic diagram of four-layer function-based tropospheric tomography

147

148 *B-spline function*

149 Due to the spatial variations of water vapor and considering the local modeling ability of different
 150 functions, the B-spline function is used as the base function for regional modeling of the WVD.
 151 B-spline is a special kind of wavelet that presents useful and remarkable properties such as
 152 symmetry, simplicity, semi-orthogonality, and compact support (Amerian et al. 2013a). The
 153 normalized B-spline scaling function is as follows:

$$154 \quad \phi_{J,k}(x) = N_{J,k}^d(x) = \frac{x-t_k^J}{t_{k+d}^J - t_k^J} N_{J,k}^{d-1}(x) + \frac{t_{k+d+1}^J - x}{t_{k+d+1}^J - t_{k+1}^J} N_{J,k+1}^{d-1}(x) \quad (12)$$

155 where d is degree of function, J is resolution level, k is shift and x is variable. The scaling function
 156 space has $K_J = 2^J + d$ basis functions. It should be noted that when the denominators of (12) are
 157 zero, the fraction will be considered zero (Amerian et al. 2013a). The required initial values can
 158 be obtained using:

$$159 \quad N_{J,k}^0(x) = \begin{cases} 1 & \text{if } t_k^J \leq x \leq t_{k+1}^J \\ 0 & \text{otherwise} \end{cases} \quad (13)$$

160 where $k = 0, 1, \dots, K_J - 1$ are shift values and $t_0, t_1, \dots, t_{K_J+d}$ is a sequence of spaced values called knots.

$$161 \quad t_0, t_1, \dots, t_{K_J+d} = \frac{1}{2^J} \left(\underbrace{0, \dots, 0}_{d+1 \text{ times}}, 1, 2, \dots, 2^J - 1, \underbrace{2^J, \dots, 2^J}_{d+1 \text{ times}} \right) \quad (14)$$

162 In this method, endpoint-interpolating B-spline on unit interval $[0,1]$ is used to avoid the edge
 163 effect at the boundaries. For this aim, the first and last $d+1$ knots are set to zero and one,
 164 respectively (Mautz et al. 2005; Amerian et al. 2013a; Amerian et al. 2013b).

165 The WVD in each layer is expanded into 2D B-spline scaling function $\phi_{J_1, J_2, k_1, k_2}(\lambda, \varphi)$ with
 166 unknown scaling coefficients C_{J_1, J_2, k_1, k_2} :

$$167 \quad \rho_i = \sum_{k_1=0}^{K_{J_1}-1} \sum_{k_2=0}^{K_{J_2}-1} C_{J_1, J_2, k_1, k_2} \phi_{J_1, J_2, k_1, k_2}(\lambda_i, \varphi_i) \quad (15)$$

168 The 2D B-spline scaling function can be computed using the tensor product of 1D functions:

$$169 \quad \phi_{J_1, J_2, k_1, k_2}(\lambda, \varphi) = \phi_{J_1, k_1}(\lambda) \phi_{J_2, k_2}(\varphi) \quad (16)$$

170 Finally, the tropospheric tomography based on 2D B-spline scaling function is expressed as
 171 follows:

$$172 \quad SWV^P = (d_1^P \cdot \sum_{k_1=0}^{K_{J_1}-1} \sum_{k_2=0}^{K_{J_2}-1} C^1_{J_1, J_2, k_1, k_2} \phi_{J_1, J_2, k_1, k_2}(\lambda_1, \varphi_1)) + \dots + (d_n^P \cdot \sum_{k_1=0}^{K_{J_1}-1} \sum_{k_2=0}^{K_{J_2}-1} C^n_{J_1, J_2, k_1, k_2} \phi_{J_1, J_2, k_1, k_2}(\lambda_n, \varphi_n)) \quad (17)$$

173 This system of equations can be written in the following form:

$$174 \quad L = A x \quad (18)$$

175 where L is the observation vector, A is the coefficient matrix that includes the base functions and
176 distance traveled by the rays in each layer, and x is an unknown vector that includes the B-spline
177 scaling coefficients. The B-spline scaling function provides local support, and not all observations
178 will contribute to the estimation of an unknown. Therefore, the coefficient matrix A is a sparse
179 matrix. In this method, it is necessary to use a prior constraint in order to reconstruct the vertical
180 distribution of water vapor properly. For this purpose, the radiosonde measurements at various
181 layers have been used. The tropospheric tomography is inherently a Fredholm integral equation of
182 the first kind. In mathematics, it has been shown that in this kind of integral equation, the output
183 is not a continuous function of the input parameters (Hansen 1997). It can be proven that inverse
184 problems based on this kind of integral equation are ill-conditioned problems, and the use of
185 regularization methods to solve them is inevitable (Hansen 1997). Similar to the voxel-based
186 approach, the LSQR iterative regularization method is used to solve the inverse problem. The 3D
187 ray-tracing technique is used to compute the distance traveled by the rays in each layer.

188

189 **Study area and data set**

190 In order to study the function-based tropospheric tomography method, a region in North America
191 has been selected (Fig.2). For a comprehensive review of the effectiveness of the proposed method,
192 17 dual-frequency GPS observations for 30 days of 2018 between July and December in different
193 weather conditions have been used. These days have been selected based on the diversity of the
194 relative humidity index. The distribution of the GPS stations and topography of the study area can
195 be seen in Figs.3 and 4. In this research, the ERA-Interim reanalysis model published by the
196 European Center for Medium-Range Weather Forecasts (ECMWF) has been used to perform 3D
197 ray-tracing technique and to select appropriate degree and level in function-based tomography.
198 The ERA-Interim reanalysis model presented values of several meteorological data on 37 pressure
199 levels. The spatial resolution of this data is about 75 km (Dee et al. 2011). These data have been
200 widely used in various aspects of geodesy and remote sensing (Haji-Aghajany et al., 2017; Haji-
201 Aghajany et al., 2019). The results are validated using observations from the radiosonde station in
202 the area in addition to the positioning technique.

203

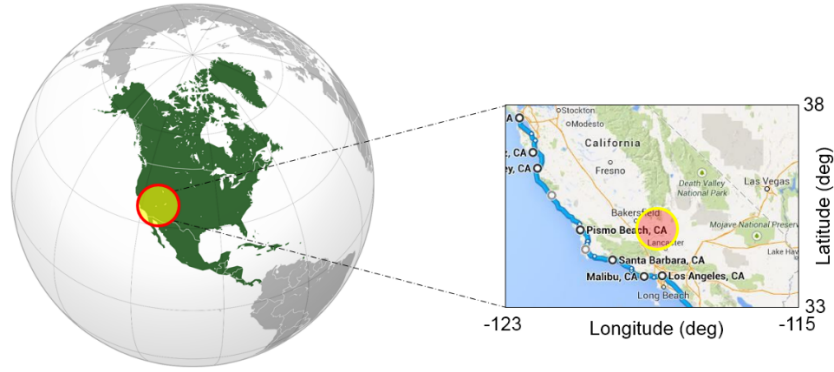


Fig. 2 Geographical location of the study area

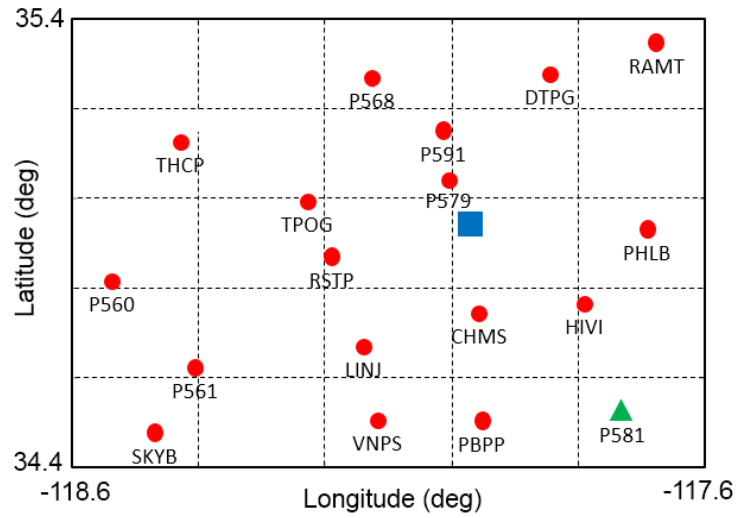
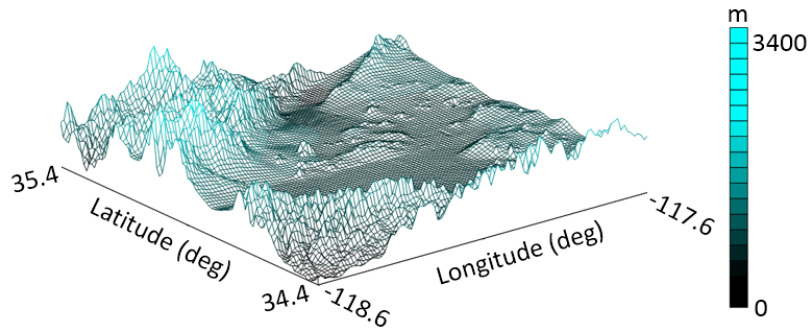


Fig. 3 Distribution of the GPS stations. The blue square represents the radiosonde station, and the green triangle shows the position of the station used to evaluate the results



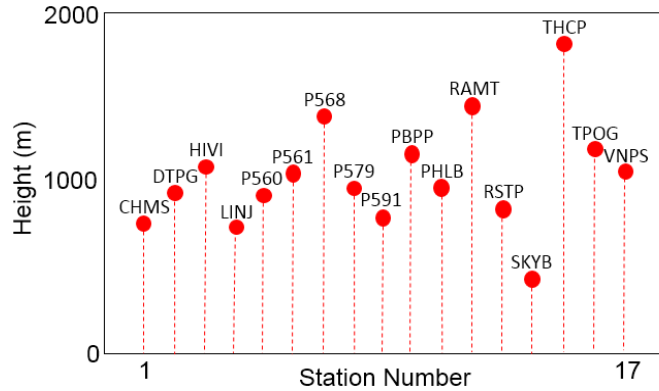


Fig. 4 Topography of the study area and vertical distribution of the GPS stations.

Data processing and results

The GPS observations have been processed using Bernese 5.2 software to estimate the tropospheric delay (Dach et al. 2015). First, the RNXSMT program has been used to detect cycle slip and outlier. The next step was to convert the RINEX (Receiver Independent Exchange) ASCII format observation files format to the software format using RXOBV3 program. Then, the standard orbits have been created using PRETAB and ORBGEN programs. CODSP and MAUPRP programs have been used for clock synchronization and to resolve cycle slip and multipath, respectively. Finally, GPSEST program has been used to parameter determination (Dach et al. 2015). The ionosphere-free linear combination, a ZTD interval of 30 minutes and gradients interval in north-south and east-west directions of 2 hours have been considered for this processing. The global mapping function (GMF) has been used to convert the zenith direction to slant direction (Bohm and Niell, 2006). Examples of obtained ZTDs can be seen in Fig.5. The different behavior of the delay in these stations are due to the topography of the area and different weather conditions.

The RESRMS program can be used to screen the post-fit residuals produced in a GPSEST run to identify outliers. In the following, the results of voxel-based and function-based tomography are presented.

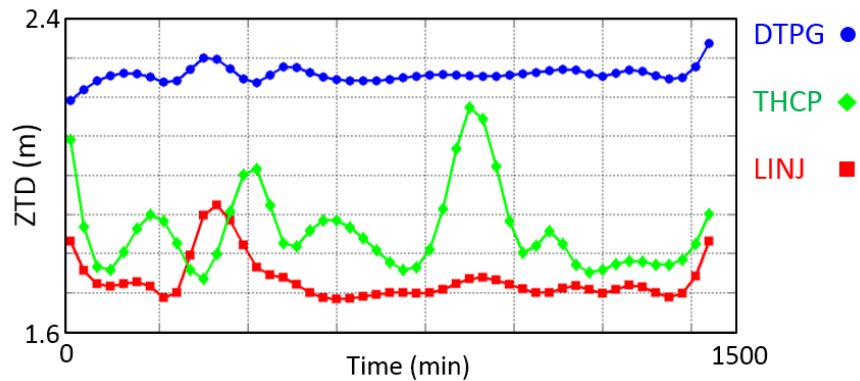


Fig. 5 Computed ZTD for the three sample stations on one of the processing days

232

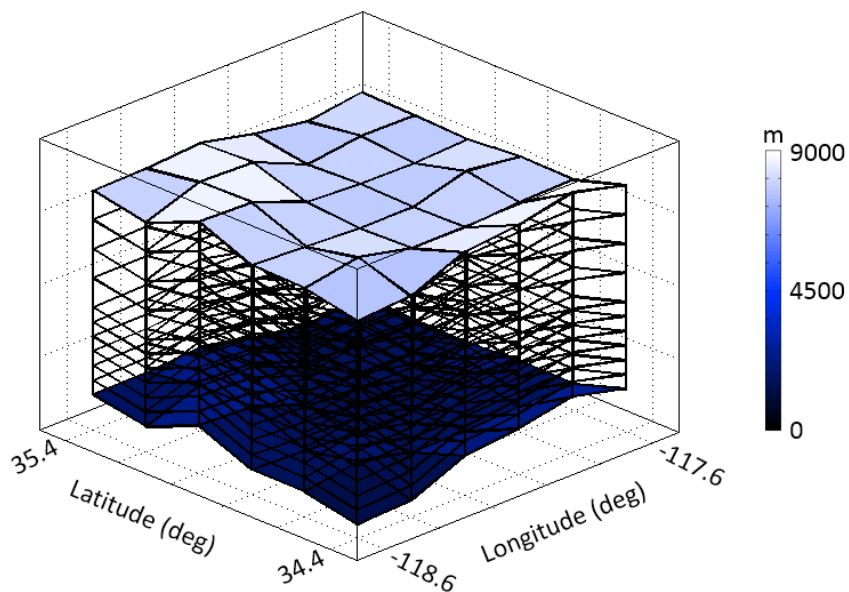
233

234

235 Voxel-based tomography results

236 One of the most important steps of voxel-based tropospheric tomography is selecting the optimum
 237 horizontal and vertical resolution for the model according to the topography of the study area. The
 238 model resolution matrix is one of the characteristics of the coefficient matrix and reflects the
 239 geometry and optimal resolution of the tomography model (Bender et al. 2011; Haji-Aghajany and
 240 Amerian. 2017). According to the resolution matrix, the horizontal resolution of 0.2 degrees has
 241 been chosen for the tomography model (Fig.6). The vertical resolution for the first 6 layers is 500
 242 meters. This resolution is reduced to 1000 meters for the next 4 layers in the figure.

243



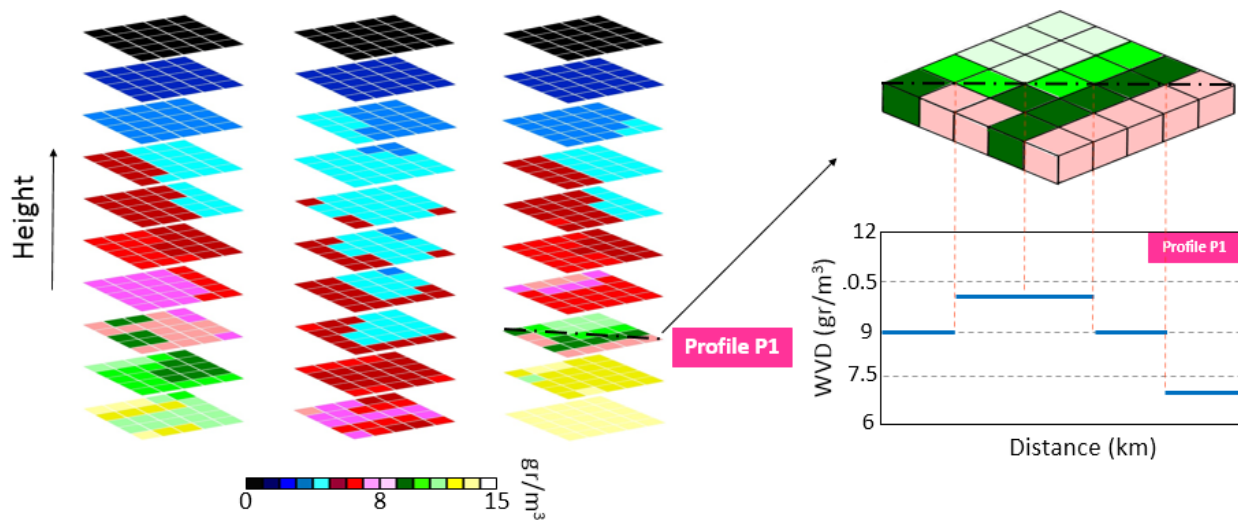
244

245 **Fig. 6** 3D voxel-based tomography model

246

247 Based on all the above, the 3D WVD fields have been reconstructed for 30 days under
248 different weather conditions. The voxel-based tropospheric tomography results of this research
249 have a temporal resolution of 30 min following the temporal resolution of the estimated
250 tropospheric delay. An example of the obtained WVD field in different layers can be seen in Fig.7.
251 The WVD has an irregular spatiotemporal distribution due to the advection, turbulence and
252 transport. The distribution of the WVD in vertical layers for three epochs is well visible in the
253 figure. It is correctly seen that the WVD decreases with increasing height. The important point in
254 the figure is that the WVD is the same everywhere in the 3D space of a voxel.

255



256

257 **Fig. 7** Example of reconstructed WVD field for three different epochs (07/08/2018-03/10/2018-
258 02/11/2018). The plotted profile shows that the reconstructed water vapor obtained from this
259 method is constant in each voxel

260

261 Function-based tomography results

262 In order to perform function-based tropospheric tomography, we have considered the vertical
263 resolution of the model following the previous method. The most important step in the function-
264 based tropospheric tomography is to select the optimal degree and level of the B-spline function.

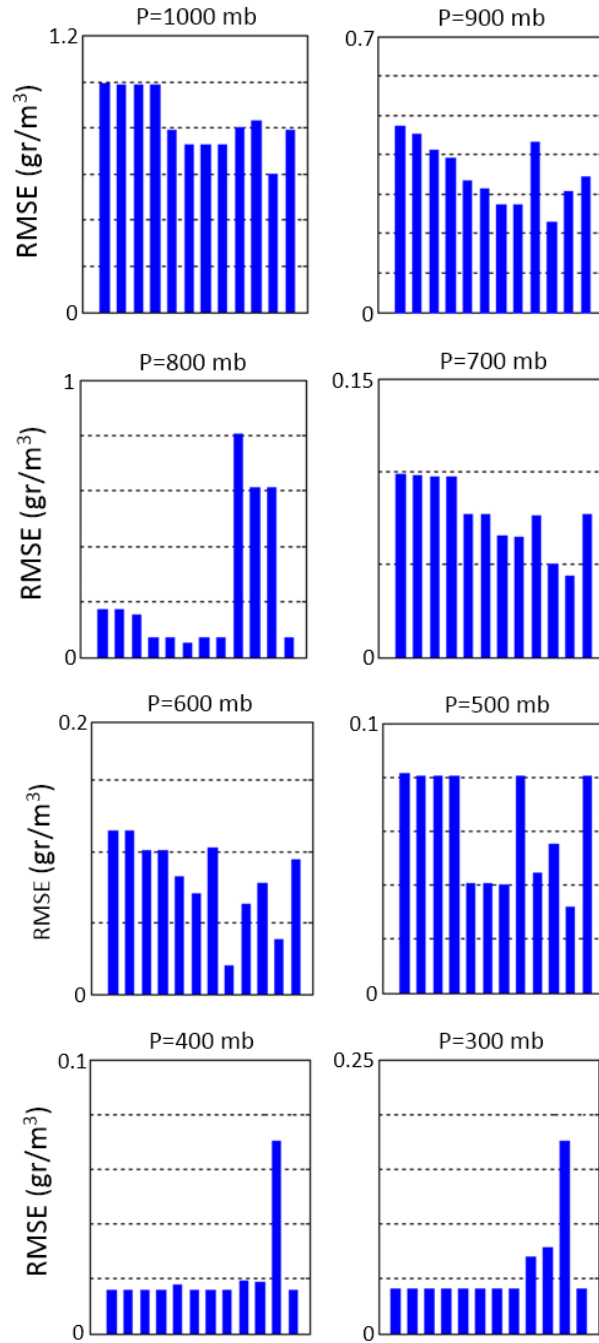
265 The spatial distribution of WVD varies at different height levels. At higher vertical layers, the
266 spatial variations of WVD are smoother compared to the lower layers. Therefore it is necessary to
267 use different degrees and levels of B-spline function in each layer for better modeling of WVD as
268 well as better management of the number of unknown parameters. The ERA-Interim model has
269 been used to determine the appropriate degree and level in different vertical layers. For this
270 purpose, the B-spline functions with different degrees and levels have been fitted to one year of
271 ERA-Interim data, and then the coefficients of the functions have been computed. The ERA-
272 Interim data of 10 days in different weather conditions and different average relative humidity
273 have been used to evaluate different degrees and levels of the function in various vertical layers.
274 Fig.8 shows the comparison of the average Root Mean Square Error (RMSE) between the obtained
275 WVD using the function coefficients and the ERA-Interim data which indicates the model misfit.

276 Based on these results and considering the number of unknown parameters produced by
277 the B-spline function, the optimal degrees and levels of the function in different vertical layers
278 have been chosen to perform the method. Figure 9 shows the intended degree and level and the
279 number of unknown parameters in each layer.

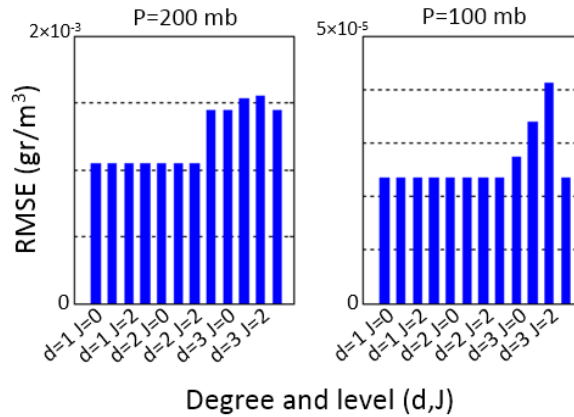
280 Figure 10 shows the example of the estimated WVD field in vertical layers for three
281 different epochs using the B-spline function-based method in the study area. The 2D distribution
282 of WVD and profile plotted in the figure shows that the function-based tomography models results
283 are more detailed and continuous compared to the general and discrete results of the voxel-based
284 method. In order to compare the two methods and to obtain more precise conclusions, the obtained
285 results should be validated.

286

287



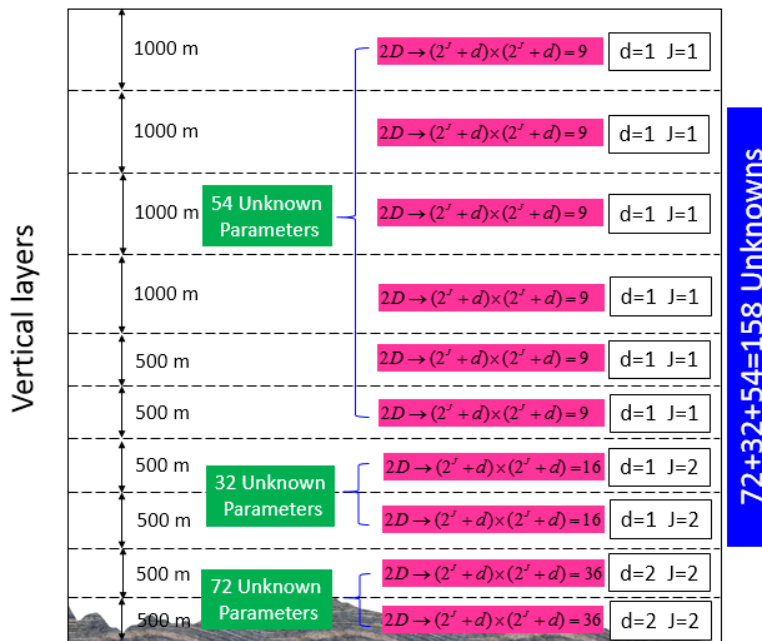
288



289

290 **Fig. 8** Comparison between obtained average RMSE from different degrees and levels at some
 291 pressure levels. This comparison shows that the average RMSE decreases with decreasing
 292 pressure.

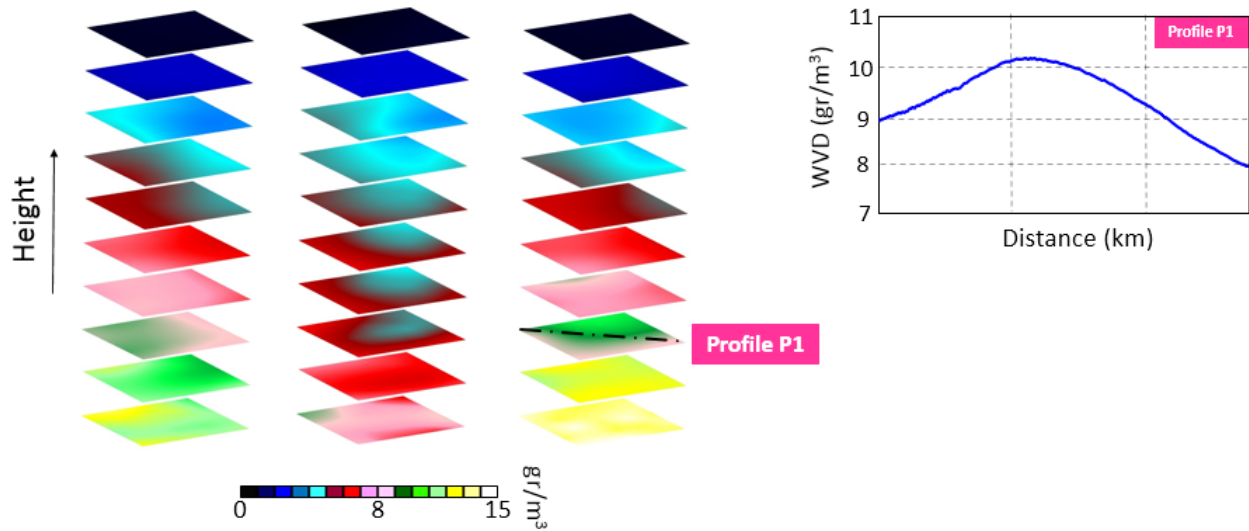
293



294

295 **Fig. 9** Schematic diagram of the considered layer and the number of unknown parameters

296



297

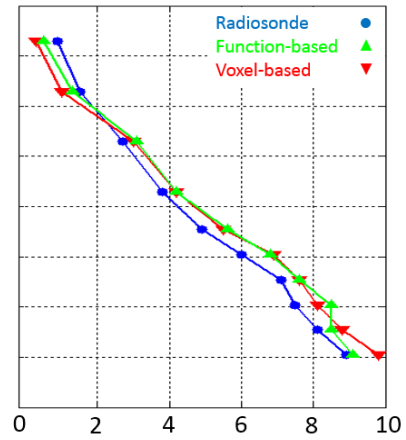
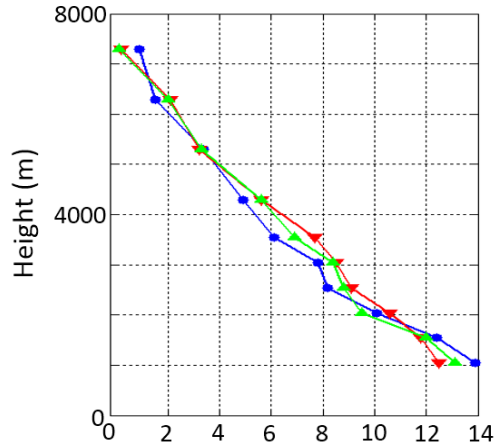
298 **Fig. 10** Example of obtained WVD field for three different epochs (07/08/2018-03/10/2018-
 299 02/11/2018).

300 **Validation of the tomography modeling**

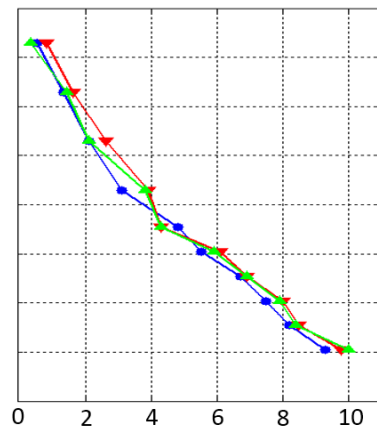
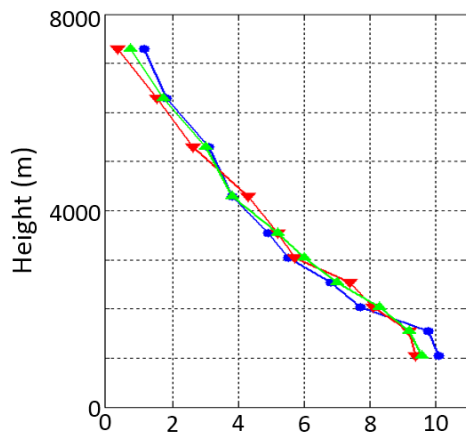
301 Radiosonde observations can provide accurate WVD profiles. Therefore, the use of these data is
 302 one of the most common ways to validate the results of tropospheric tomography. Radiosonde
 303 balloons are usually launched daily at 00:00 and 12:00 UTC. There is a radiosonde station located
 304 in the study area. In order to validate the WVD from voxel-based and functioned-based methods,
 305 we compared the results for the location of the radiosonde station with radiosonde data (as
 306 reference) for the experimental period of 30 days. Examples of this comparison for six different
 307 epochs are visible in Fig.11. The reconstructed WVD is generally consistent with radiosonde
 308 measurements. However, at some altitudes, significant differences between the obtained WVD and
 309 validation data are visible. The maximum differences between the reconstructed WVD and the
 310 radiosonde measurements are visible in the lower and middle vertical layers. Table.1 shows the
 311 statistical parameters between the results of tropospheric tomography methods and radiosonde data
 312 over the tested period. The scatter plot has been used to better compare the obtained WVD (Fig.12).

313

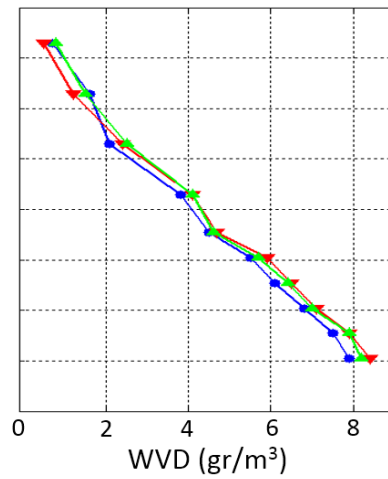
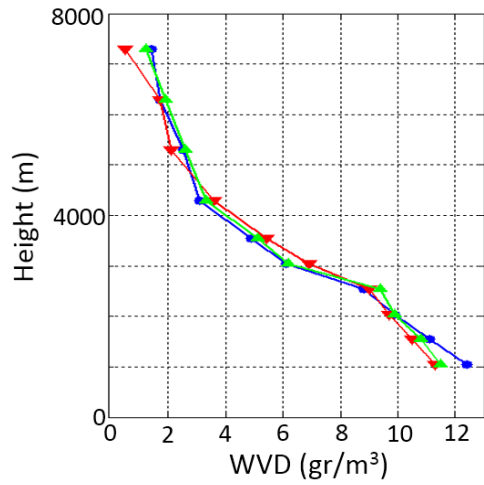
314



315



316



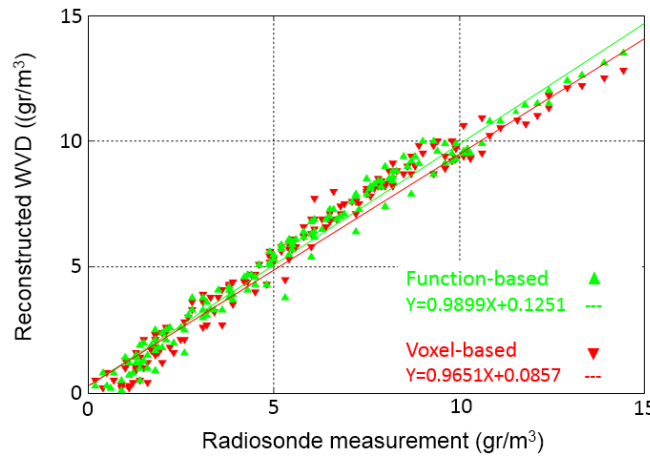
317 **Fig. 11** Examples of comparison between reconstructed WVD and radiosonde measurements for
 318 three different epochs (07/08/2018-03/10/2018-02/11/2018).

319

320 **Table1** Statistical comparison between the reconstructed WVD and radiosonde validation data

Method	RMSE (gr/m ³)	Bias (gr/m ³)	Min-Diff (gr/m ³)	Max-Diff (gr/m ³)
Function-based	0.61	-0.14	0.06	0.91
Voxel-based	0.89	-0.15	0.11	1.62

321



322

323

Fig. 12 Scatter plot between reconstructed WVD and radiosonde observations

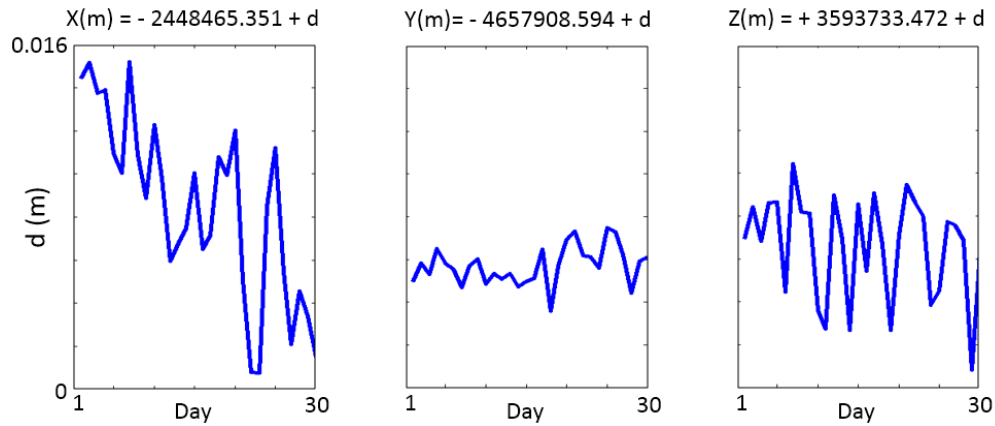
324

325 The statistical results in Table.1 and the slope of the fitted lines in Fig.12 show that the
 326 results obtained from the two approaches are close to each other, although the results of the
 327 function-based method are closer to the radiosonde observations. The used radiosonde station is
 328 located in the middle of the study area, so the obtained results on the boundary voxels of the
 329 tomography model cannot be validated using this station. On the other hand, in order to compare
 330 these two methods more precisely, it is necessary to examine the results on the sides of the
 331 tomography model. Therefore, the precise point positioning (PPP) technique has been used for this
 332 purpose.

333 One GPS station in the selected area has been used for this validation. It should be noted that this
 334 station has not been used in the tomography process. First, the position time series of this station
 335 on the days of tomography has been obtained from the Plate Boundary Observatory (PBO) GPS

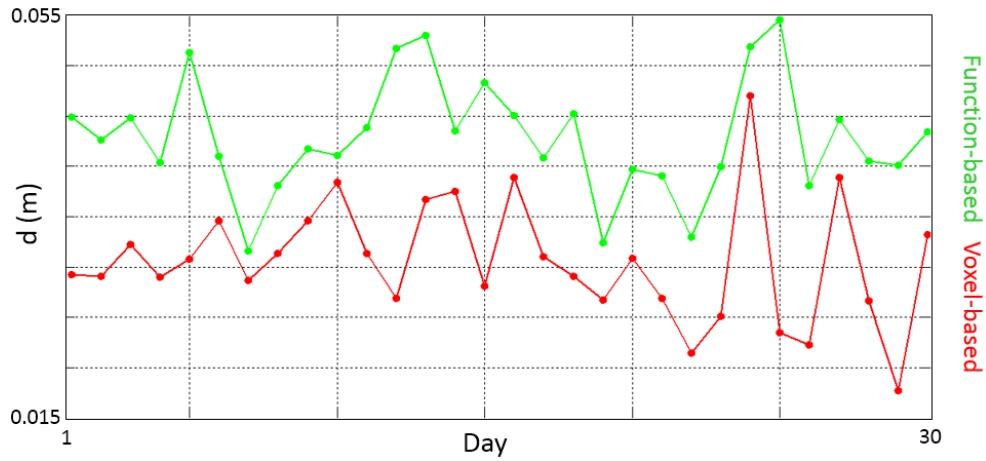
336 network (<http://unavco.org>). Fig.13 shows the time series of the position components of this
 337 station. The SWD and slant hydrostatic delay (SHD) of GPS observations has been estimated using
 338 reconstructed water vapor from two tomography methods and saastamoinen model, respectively.
 339 Then, the observations of the GPS station have been corrected using these corrections. After this
 340 step, positioning has been performed again using the PPP technique. Previous studies have proven
 341 that the discrepancy between tropospheric effect correction methods is more noticeable in wet
 342 weather conditions. Therefore, the comparison has been made in two types of weather conditions.
 343 The first category includes days with an average humidity of more than 50%, and the second group
 344 includes days with an average humidity of less than 50%. This classification has been done based
 345 on the ERA-Interim data. Fig.14 shows the comparison between obtained 3D positions from two
 346 tomography methods. Finally, the RMSE between the positions obtained using the two
 347 tomography methods and the position obtained from the PBO GPS network has been computed
 348 (Fig.15, Table.2).

349



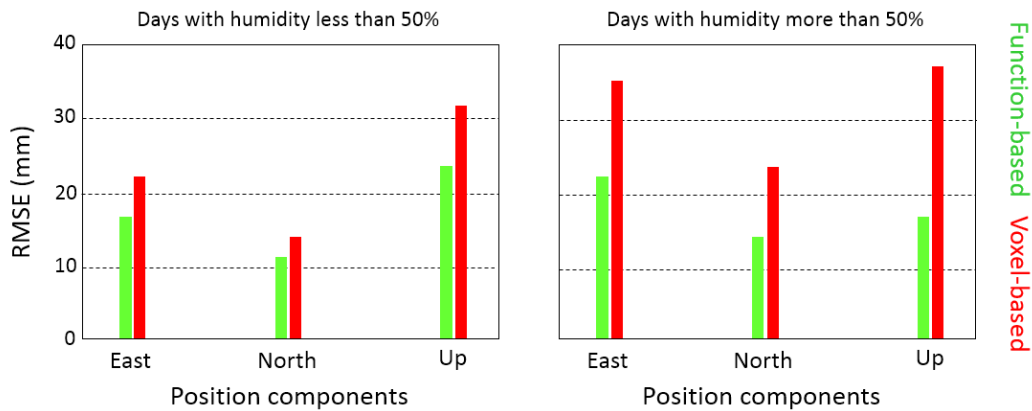
351

Fig. 13 Position time series of this station



352
353
354
355

Fig. 14 3D difference between obtained positions from two tomography methods and the positions obtained from the PBO GPS network



356
357
358
359

Fig. 15 RMSE in different weather condition

Table2 Comparison of the obtained RMSE

	RMSE in Days with humidity less than 50% (mm)			RMSE in Days with humidity more than 50% (mm)		
	East	North	Up	East	North	Up
Function-based	16.92	11.83	23.58	22.12	14.47	17.51
Voxel-based	22.71	14.87	31.97	35.86	23.53	37.71

360

361 On days with humidity less than 50%, the difference between obtained RMSE in
362 computing the Up component is about 9 mm. This difference is statistically significant. However,
363 the obtained RMSE of the East and North components for both tomography methods is very close
364 to each other, and there is some improvement in the accuracy of the results. This comparison shows
365 that accuracy improvement in the vertical component is more significant than in the horizontal
366 components.

367 On days with humidity more than 50%, the conclusion is quite different. The difference
368 between the RMSE in East, North and Up components is about 14, 10 and 20 mm, respectively.
369 Considering the accuracy of the PPP technique, these differences are significant and cannot be
370 ignored. The highest and lowest differences are observed in the Up and East components. On the
371 basis of Fig.14, it can be generally said that the effect of using the method to increase the accuracy
372 of the Up and East components are significant.

373 Based on all these validations, it can be concluded that using the function-based method
374 based on B-spline function can increase the ability of the tomography technique compared to the
375 voxel-based method.

376

377 **Conclusion**

378 We presented a new tropospheric tomography approach based on the B-spline function and its
379 ability was validated under different weather conditions. This function-based method divided the
380 research area for some layers vertically while the WVD function was introduced horizontally,
381 rather than discretized the research area into many voxels as performed by the voxel-based method.
382 Using the function-based tropospheric tomography, we can neglect the empirical constraints. This
383 method only uses an a priori constraint. The empirical constraints have an unfavorable effect on
384 voxel-based tomography results due to the unsuitable relationship between voxels in vertical and
385 horizontal directions. The proposed method also reduces the number of unknown parameters
386 because it estimates only the coefficients of the WVD function in each vertical layer. Therefore,
387 this method can overcome the rank deficiency problem in tropospheric tomography resolution. It
388 was observed that using the function-based method, the WVD can be reconstructed continuously
389 in each vertical layer, unlike the voxel-based method. The results of two tomography methods
390 were compared using radiosonde observations and the PPP technique. Validation using radiosonde

391 showed that the function-based method is more accurate in reconstructing the water vapor.
392 However, the results of the two methods were close to each other. Next, the PPP technique was
393 used to evaluate the results near the edge of the tomography model. The results of this validation
394 showed that the PPP with a priori data from function-based tomography has better accuracy of the
395 position components (especially Up) than if we take them from voxel-based tomography.

396

397 **Acknowledgments**

398 The authors would like to appreciate the UNAVCO for the GPS observations and for providing
399 high-accuracy station position time series. We are also grateful to the ECMWF for publishing
400 ERA-Interim data.

401

402 **Data Availability**

403 The datasets generated during and/or analyzed during the current study are not publicly available
404 but are available from the corresponding author on reasonable request.

405

406 **References**

407 Amerian Y, Hossainali MM, Voosoghi B., (2013a). Regional improvement of IRI extracted
408 ionospheric electron density by compactly supported base functions using GPS observations.
409 J Atmos Sol Terr Phys 92:23–30. doi: 10.1016/j.jastp.2012.09.011.

410 Amerian, Y., Voosoghi, B., Mashhadi Hossainali, M., (2013b). Regional Ionosphere Modeling in
411 Support of IRI and Wavelet Using GPS Observations. Acta Geophysica. 61(5):1246-1261,
412 DOI: 10.2478/s11600-013-0121-5.

413 Bender, M., Dick, G., Ge, M., Deng, Z., Wickert, J., Kahle, H.-G., Raabe, A., and Tetzlaff, G.,
414 (2011). Development of a GNSS water vapour tomography system using algebraic
415 reconstruction techniques, Adv. Space Res., 47, 1704–1720.

416 Bevis, M., Businger, S., Herring, T. A., Rocken, C., Anthes, R. A., Ware, R. H., (1992). GPS
417 meteorology: Remote sensing of atmospheric water vapor using the Global Positioning
418 System. Journal of Geophysical Research: Atmospheres, 97(D14): 15787-15801.

419 Böhm, J.; Niell, A.; Tregoning, P.; Schuh, H. Global Mapping Function (GMF): A new empirical
420 mapping function based on numerical weather model data. *Geophys. Res. Lett.* 2006, 33, 1-
421 4.

422 Braun, J.J., (2004). Remote sensing of atmospheric water vapor with the global positioning system
423 (Ph.D.). University of Colorado.

424 Chen BY, Liu ZZ., (2014). Voxel-optimized regional water vapor tomography and comparison
425 with radiosonde and numerical weather model. *J Geod* 88(7):391–703. doi:10.1007/s00190-
426 014- 0715-y.

427 Dach, R., S. Lutz, P. Walser, P. Fridez (Eds)., (2015). Bernese GNSS Software Version 5.2. User
428 manual, Astronomical Institute, University of Bern, Bern Open Publishing. DOI:
429 10.7892/boris.72297; ISBN: 978-3-906813-05-9.

430 J. L. Davis, G. Elgered, A. E. Niell, and C. E. Kuehn., (1993). Ground-based measurement of
431 gradients in the wet radio refractivity of air. *Radio Sci.*, vol. 28, pp. 1003–1038.

432 Dee, D.P., et al., (2011) The ERA-Interim reanalysis: configuration and performance of the data
433 assimilation system, *Q. J. R. Meteorol. Soc.* 137(656): 553–597, doi: 10.1002/qj.828.

434 Flores, A., Ruffini, G., and Rius, A., (2000). 4D tropospheric tomography using GPS slant wet
435 delays, *Ann. Geophys. Ger.*, 18(2):223–234.

436 Haji-Aghajany. S, B. Voosoghi, and A. Yazdian., (2017). Estimation of North Tabriz Fault
437 Parameters Using Neural Networks and 3D Tropospherically Corrected Surface Displacement
438 Field. *Geomatics, Natural Hazards and Risk* 8 (2): 918–932.
439 doi:10.1080/19475705.2017.1289248.

440 Haji-Aghajany, S., Amerian, Y., (2017). Three dimensional ray tracing technique for tropospheric
441 water vapor tomography using GPS measurements. *Journal of Atmospheric and Solar-
442 Terrestrial Physics.* 164, 81-88. doi: 10.1016/j.jastp.2017.08.003.

443 Haji-Aghajany, S., Amerian, Y., (2018). Hybrid Regularized GPS Tropospheric Sensing Using 3-
444 D Ray Tracing Technique. *IEEE Geoscience and Remote Sensing Letters.* 15(10):1475-1479.
445 doi: 10.1109/LGRS.2018.2853183.

446 Haji-Aghajany. S, B. Voosoghi, and Y. Amerian., (2019). “Estimating the slip rate on the north
447 Tabriz fault (Iran) from InSAR measurements with tropospheric correction using 3D ray
448 tracing technique.” *Advance in space research*. Volume 64, Issue 11, Pages 2199-2208. Doi:
449 <https://doi.org/10.1016/j.asr.2019.08.021>.

450 Hansen, P.C., (1997). Rank-deficient and Discrete Ill-posed Problems. Numerical Aspects of
451 Linear Inversion, Monographs on Mathematical Modeling and computation, Vol. 4, SIAM,
452 Philadelphia

453 Heublein, M., Alshawaf, F., Erdn, Ba., Zhu, X., Hinz, S., (2019). Compressive sensing
454 reconstruction of 3D wet refractivity based on GNSS and InSAR observations, *Journal of*
455 *Geodesy*, 93(2):197-217. <https://doi.org/10.1007/s00190-018-1152-0>.

456 Hirahara K., (2000). Local GPS tropospheric tomography, *Earth Planet. Space*, 52:935–939.

457 Mautz,R., Ping,J., Heki,K., Schaffrin,B., Shum,C.K., Potts,L.,2005. Efficient spatial and temporal
458 representations of global ionosphere maps over Japan using B-spline wavelets. *Journal of*
459 *Geodesy* 78,660–667.

460 Perler D, Geiger A, (2011). Hurter F. 4D GPS water vapor tomography: new parameterized
461 approaches. *J Geodesy*, 85:539-550.

462 Merrikhpour, M., Rahimzadegan, M., (2017). Improving the Algorithm of Extracting Regional
463 Total Precipitable Water Vapor Over Land From MODIS Images. *IEEE Transactions on*
464 *Geoscience and Remote Sensing*, 55(10):5889-5898. doi: 10.1109/TGRS.2017.2716414.

465 Merrikhpour, M., Rahimzadegan, M., 2019. Analysis of temporal and spatial variations of total
466 precipitable water vapor in western Iran using radiosonde and MODIS measurements, *Journal*
467 *of Applied Remote Sensing* 13(4). <https://doi.org/10.1117/1.JRS.13.044508>.

468 Rohm, W. and Bosy, J., (2009). Local tomography troposphere model over mountains area, *Atmos.*
469 *Res.*, 93:777–783.

470 Rohm W, Zhang K, Bosy J., (2014). Limited constraint, robust Kalman filtering for GNSS
471 troposphere tomography. *Atmos Meas Tech*, 6:1475-1486.

472 Saastamoinen, J., (1973). Contributions to the theory of atmospheric refraction. Part II: refraction
473 corrections in satellite geodesy. *Bull. Geod.* 107:13–34.

474 Troller, M., Burki, B., Cocard, M., Geiger, A., Kahle, H. G., (2002). 3-D refractivity field from
475 GPS double difference tomography, *Geophys. Res. Lett.*, 29, 2-1–2-4.

476 Yao Y, Zhao Q., (2016). Maximally Using GPS Observation for Water Vapor Tomography. *IEEE*
477 *T Geosci Remote*, 54, 7185-7196.

478 Zhao, Q., & Yao, Y. (2017). An improved troposphere tomographic approach considering the
479 signals coming from the side face of the tomographic area. *Annales Geophysicae*, 35(1), 87-
480 95.

481 Zhao, Q. Z., Yao, Y. B., Cao, X. Y., Zhou, F., and Xia, P., (2018a). An optimal tropospheric
482 tomography method based on the multi-GNSS observations, *Remote Sensing*, 10, 1–15.

483 Zhao, Q.; Yao, Y.; Yao, W., (2018b). Troposphere Water Vapour Tomography: A Horizontal
484 Parameterised Approach. *Remote Sens.* 10:1241.

485 Zhao, Q., Zhang K., Yao, Y., and Li, X., and Yao, W. (2019). A new troposphere tomography
486 algorithm with a truncation factor model (TFM) for GNSS networks, *GPS Solutions*,
487 2019,23:64,DOI:10.1007/s10291-019-0855-x.

488 Zhao, Q., Yao, W., Yao, Y., Li, X. (2020). An improved GNSS tropospheric tomography method
489 with the GPT2w model. *GPS Solut* 24, 60. <https://doi.org/10.1007/s10291-020-0974-4>.

490

491 **Author Biographies**



Saeid Haji-Aghajany is currently a Ph.D. candidate under the supervision of Dr. Yazdan Amerian at K. N. Toosi University of Technology, Tehran, Iran. He is also a researcher under the supervision of Dr. Sandra Verhagen at the Delft University of Technology. His main research interests include GNSS meteorology, GNSS remote sensing and deformation monitoring using GPS and InSAR observations.

502

503



Yazdan Amerian received his B.Sc. degree in geomatics engineering from the University of Tehran and his M.Sc. and Ph.D. degrees in geodesy from K. N. Toosi University of Technology, Tehran, Iran. He is now an assistant professor with the Faculty of Geodesy and Geomatics Engineering, K. N. Toosi University of Technology. His main research interests include satellite geodesy, GNSS, GNSS remote sensing.

513



Sandra Verhagen obtained her Ph.D. from and is now an assistant professor at the Delft University of Technology. Her research focuses on ambiguity resolution and integrity monitoring for real-time kinematic GNSS applications.